INLET GAP EFFECT ON TONAL NOISE GENERATED FROM A VOLUTELESS CENTRIFUGAL FAN

Martin OTTERSTEN[1,2], Hau-Dong YAO[2], Lars DAVIDSON[2]

[1] *Swegon operations, Box 336, SE-40125 Gothenburg, Sweden*

[2] *Chalmers University of Technology, Division of Fluid Dynamics, Department of Mechanics and Maritime Science, Chalmersplatsen 4, SE-41296 Gothenburg, Sweden*

SUMMARY

In this study, three voluteless centrifugal fans are compared for their aeroacoustic performances. The tonal noise is predicted by coupling the IDDES with Formulation 1A of Farassat. The sources of the tonal noise at the blade passing frequency (BPF) are identified. It is found that the sources are related to the fan inlet gap that introduces the turbulence interacting with the blade leading edge. By redesigning the gap, the tonal noise at the BPF is reduced effectively.

INTRODUCTION

Today most people spend the majority of their time indoors. The indoor environmental quality (IEQ) has become more and more important. When considering IEQ we usually think about temperature, CO_2 level, and humidity. However, it has been noticed that sound quality is an important factor for good comfort in the indoor environment [1, 2].

Nowadays a ventilation system is usually driven by a voluteless centrifugal fan, which has a gap between the rotating fan front shroud and the stationary inlet duct. The pressure difference between the inner and outer sides of the fan drives air to pass through the gap. As clarified by Hariharan and Govardhan [3], increasing the gap width worsens the blade aerodynamic performance.

There are some previous studies on voluteless centrifugal fans. It was found in both simulations and experiments for a voluteless fan [4], that the tonal noise at BPF is generated from a helical unsteady inlet vortex that interacts with the rotating blades near the fan backplate. Another cause is inflow distortion, which leads to flow separation at the blade root near the backplate [5]. Schaeffer and Boehle [6] found that the accuracy of the noise prediction, especially at BPF, is improved when the mesh is refined at the gap and the fan outlet. However, they provided no discussions on the physical

mechanisms that are associated with the improved accuracy. In a recent study, the present authors found that for a voluteless centrifugal fan, the tonal frequencies associated with the *BPF*, are related to surface pressure fluctuations at the blade leading edge (BLE) [7].

The numerical simulations in the current study are carried out using a hybrid method of the improved delayed detached eddy simulation (IDDES) [8] and the Ffowcs Williams and Hawkings (FW-H) equation [9]. The IDDES is used in the flow simulation and the FW-H is used for the noise prediction.

This study aims to investigate how the tonal noise at the *BPF* is affected when the gap is modified. Two different gap designs are compared with a reference fan (Case 1), which is the same fan in the previous study [7].

CONFIGURATION

The baseline fan (Case 1) and the two different designs (Case 2 and Case 3) are illustrated in Figure 1. Case 1 is the same fan as the one examined in [7]. The fan blades, shroud, and backplate are the same for all cases. There are 7 blades in the fan. A clearance (i.e., the gap) is located between the stationary and rotating parts. Case 2 has larger gap width (w_{case2}) and Case 3 has smaller gap width (w_{cas3}) than Case 1. The gap width is varied by changing the wall thickness of the inlet duct. As shown in Figure 1d, the fan and inlet duct are placed in a downstream duct, and the inlet duct is connected to an upstream duct. This simple geometry layout is designed for the numerical simulations. This simplification reduces the geometry complexity but retains the principal flow and acoustic characteristics. The fan and case parameters are listed in Table 1.
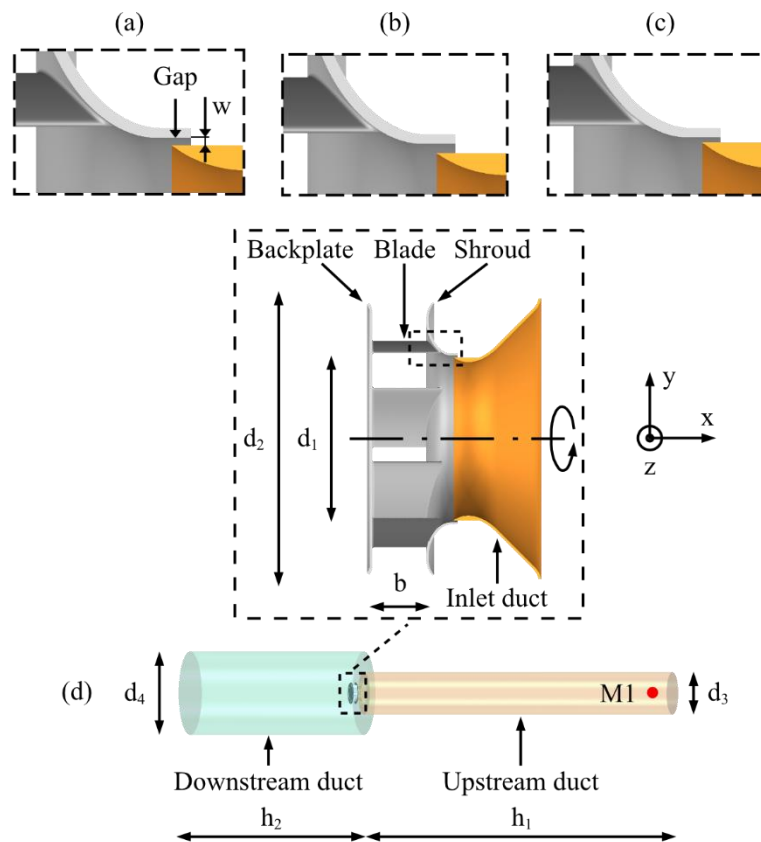

Figure 1. The fan configurations. Gray indicates the rotating fan and brown the stationary inlet duct.
a) Case 1 (baseline), b) Case 2 (with a larger gap width = w), and c) Case 3 (with a smaller gap width = w).
d) The simple geometry layout for the numerical simulations. M1 is the microphone position.
The rotation axis of the fans is the x-axis

Table 1. The fan parameters

d_1	d_2	d_3	d_4	b	h_1	h_2	w_{case1}	w_{case2}	w_{case3}
0.165 m	0.268 m	0.6 m	1.1 m	0.053 m	4.0 m	2.3 m	1.5 mm	2.0 mm	1.0 mm

The fan rotation speed is 2800 rpm. Given that the fan has seven blades, the *BPF* is 326.7 Hz. The operation point is the same as in [7], where the mass flow rate was set to 0.467 kg/s and that gave a pressure rise of 270 Pa for Case 1.

NUMERICAL METHODOLOGY

CFD method

The air is considered as an ideal gas. The flow is compressible. A finite volume method is utilized to discretize the continuity, momentum, and energy equations. The method employs a segregated flow solver accomplished with the Semi-Implicit Method for Pressure-Linked Equations (SIMPLE) algorithm. All simulations are performed using the commercial software STAR-CCM+ [10]. The turbulence is simulated using the IDDES [11] that is combined with the k-ω SST turbulence model. This setup has been tested in several studies on rotating machinery [12, 13].

FW-H equation

A hybrid approach is adopted to predict the noise generated from the flow. In this approach, the IDDES is coupled with Formulation 1A of Farassat [14]. The ambient air density is set to $\rho_0 = 1.225$ kg/m^3, and the speed of sound $c_0 = 340$ m/s.

According to Neise [15], the fan noise generation at low Mach numbers is dominated by dipole noise sources that are derived based on the FW-H equation. Hence, the noise prediction in this study considers only an impermeable integral surface for Formulation 1A. The integral surface consists of the fan blades, shroud, and backplate (see Figure 1), while the upstream and downstream ducts, as well as the fan inlet duct, are neglected. Thus, there is a limited acoustic reflection from these walls [16].

Numerical settings

The entire computational domain is divided into stationary and rotating parts. The meshes of the stationary and rotary meshes are not conformable at the interfaces between them.

The under-relaxation factors for the velocity and pressure in the segregated flow solver are set to 0.7 and 0.4, respectively. The under-relaxation factor for the turbulence equations is 0.7.

The mass-flow boundary condition is set at the inlet with a uniform velocity distribution. The modeled turbulence intensity is set to $I = 4\%$ according to $I = 0.16(R_e)^{-1/8}$ [10]. The modeled turbulence length scale is set to $\ell = 0.05$ m based on $\ell = 0.7d_3$ where d_3 is the upstream duct diameter. The pressure-outlet boundary condition is set at the outlet with the static pressure of 101 325 Pa, which is the reference pressure (p_{ref}) in the ambient air. The no-slip boundary condition is specified on all walls.

The time step is set to $\Delta t = 2.0 \times 10^{-5}$ s, leading to a maximum convective Courant number of around 10. This value fulfills the numerical stability required for the implicit time-marching method. The maximum number of inner iterations per time step is set to 12.

The sampling period of the noise is 0.3 s for all cases, corresponding to 14 fan revolutions. The sound pressure level (SPL) is calculated using the von Hann window for 3000 samples per signal section, which leads to a frequency resolution of around 3 Hz. The signal sections do not overlap each other.

MESH

We adopt the same mesh generation strategy that was developed and evaluated in [7], where the fan is the same as Case 1. A polyhedral mesh generation method was used to produce prism layers near the walls and polyhedral cells in the rest of the computation domain. The use of polyhedral cells for turbomachines has been demonstrated in [16, 17]. The growth rate is set to 1.05, as suggested in [18]. The most important findings in the mesh study performed in [7], was that a local refinement has to be made at the regions extending from the gap to the BLE and along the blade to the blade trailing edge. The mesh parameters are listed in Table 2.

Table 2. The mesh parameters

	Case 1	**Case 2**	**Case 3**
Total number of cells	52×10^6	52.2×10^6	52×10^6
Number of cells in the rotating zone	41.9×10^6	42.1×10^6	41.9×10^6
Maximum Δy^+ near blade walls	0.73	0.73	0.73
Cell growth ratio	1.05	1.05	1.05

RESULTS AND DISCUSSION

Identifying sources for tonal noise for Case 1

The contours of vorticity magnitudes $\|\vec{\omega}\|$ at the blade leading edge for Case 1 is shown in Figure 2a. There are regions with high vorticity magnitude close to the shroud. They are generated when the gap flow is mixed with the main flow. This phenomenon was also observed in previous studies [7, 19]. The black dashed line is a monitoring line positioned at the BLE which extends from the backplate to the shroud. The line follows the blade rotation and the surface pressure is monitored during 12 fan revolutions. The root mean square (RMS) of the surface pressure is shown in Figure 2b. At the position nearest the shroud, the RMS has its highest value. As the distance to the shroud increases, the RMS pressure decays. At the backplate, the RMS pressure is 160 Pa, which is approximately 25 % of the value at the shroud (700 Pa).
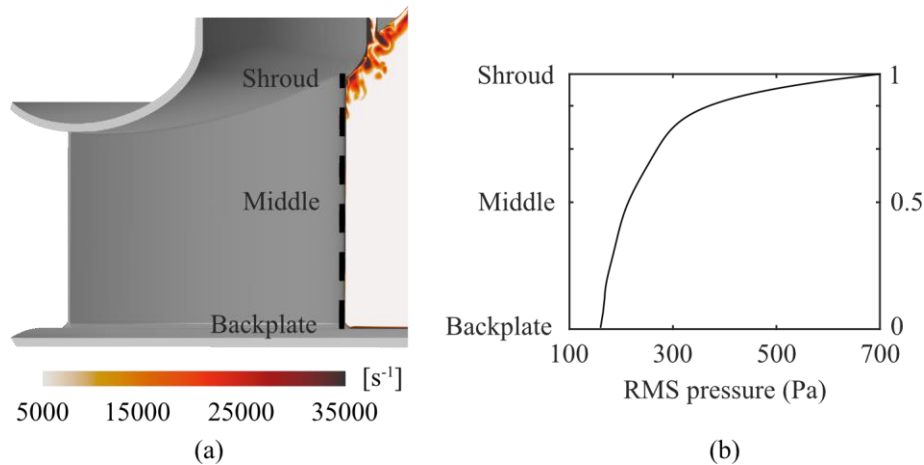

Figure 2. a) Vorticity magnitude $\|\vec{\omega}\|$ at one blade. The black dashed line marks the monitoring line at the BLE; b) the RMS of the pressure fluctuations with respect to the normalized length along the monitoring line

The time history of the surface pressure at the monitoring line are shown in Figure 3. At the position shroud, the pressure fluctuates with large amplitudes and high frequencies. As the distance from the shroud increases the amplitudes of pressure fluctuations decrease. Small fluctuations are observed at the middle position. At the backplate, fluctuations are almost negligible.

Moreover, a periodic low-frequency fluctuation in relation to the fan revolution is observed, which was also found in [20]. By comparing the three monitoring points, high-frequency fluctuations decay rapidly with increased distance to the shroud. The periodic low frequency is predominant at the middle position and at the backplate.
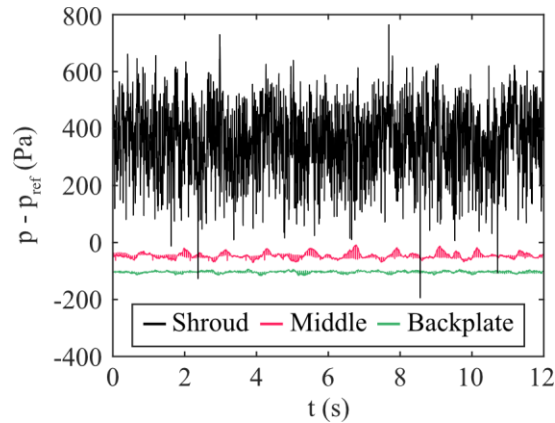

Figure 3. The time history of surface pressure fluctuations at three locations along the BLE

Based on the band-filtered SPL of the surface pressure fluctuations, the location and magnitudes of dominant tonal noise sources are evaluated. The results at the tonal frequency BPF (326.7 Hz) are illustrated in Figure 4. The location of the highest surface pressure fluctuations is at the same position (the BLE close to the shroud) as the region with high vorticity magnitudes, high RMS pressure, and largest pressure fluctuation. Hence, the interaction between inlet-gap turbulence and the BLE is responsible for the tonal noise generation. This was also shown in a previous study [7]. This approach is therefore selected when the three cases are compared in the following analysis.
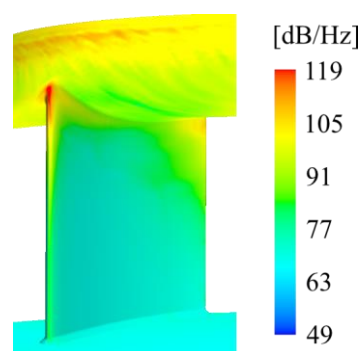

Figure 4. SPL of the tonal noise at BPF (326.7 Hz) for surface pressure fluctuations

Fan performance comparison

The static pressure excluding the reference pressure ($p_{ref} = 101325$ Pa) is displayed along the axial symmetric line for the three cases in Figure 5. All cases show similar pressure amplitudes in the upstream duct of the fan, while differences are seen downstream. Case 3 has the highest pressure and Case 2 has the lowest. The difference in the pressure rise downstream of the fan is only due to the gap design. Hariharan and Govardhan clarified [3] that when the gap width is increased, the blade aerodynamics performance is worsened. Also, when the gap width is decreased the

performance is improved, which is seen in Figure 5. According to Lee [19], a smaller gap improves the flow when it turns from axial to radial, and it also improves the flow separation conditions at the blade trailing edge.
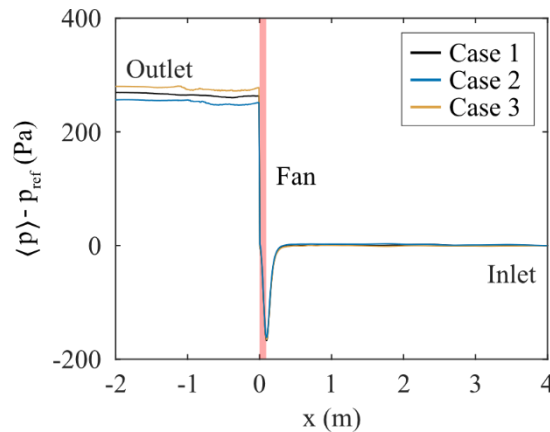

Figure 5. The pressure along the axial axis of the fan across the computational domain. Here x = -2 corresponds to the location near the outlet and x = 4 near the inlet. The fan location is marked out with the red zone

Surface pressure fluctuations comparison

The RMS pressures at the monitoring line at the BLE (described in Figure 2a) are illustrated for all cases in Figure 6a. At the position nearest the shroud, the highest RMS pressure is observed for all cases. The RMS pressures have the same physical behavior for all three cases and when the distance to the shroud increases the pressure fluctuations decay. From the shroud to the backplate, Case 2 has the lowest RMS pressure, and Cases 1 and 3 the highest. At the backplate, the cases have almost the same RMS pressure, approximately 25 % of the maximum value.

The time-average of the surface pressures at the BLE are shown at different positions for all cases in Figure 6b. The maximum values for all cases occur at the shroud, whereas at the backplate the values are negative. The amplitudes of the maximum and minimum pressure (error bar) are largest at the shroud and it decays when the distance from the shroud increases, for all cases. At the shroud, Case 1 has the highest amplitude. Case 2 has the lowest amplitudes at all positions. At point 2, the maximum positive fluctuations are larger than the magnitude of the negative ones, and it is the same for all cases.

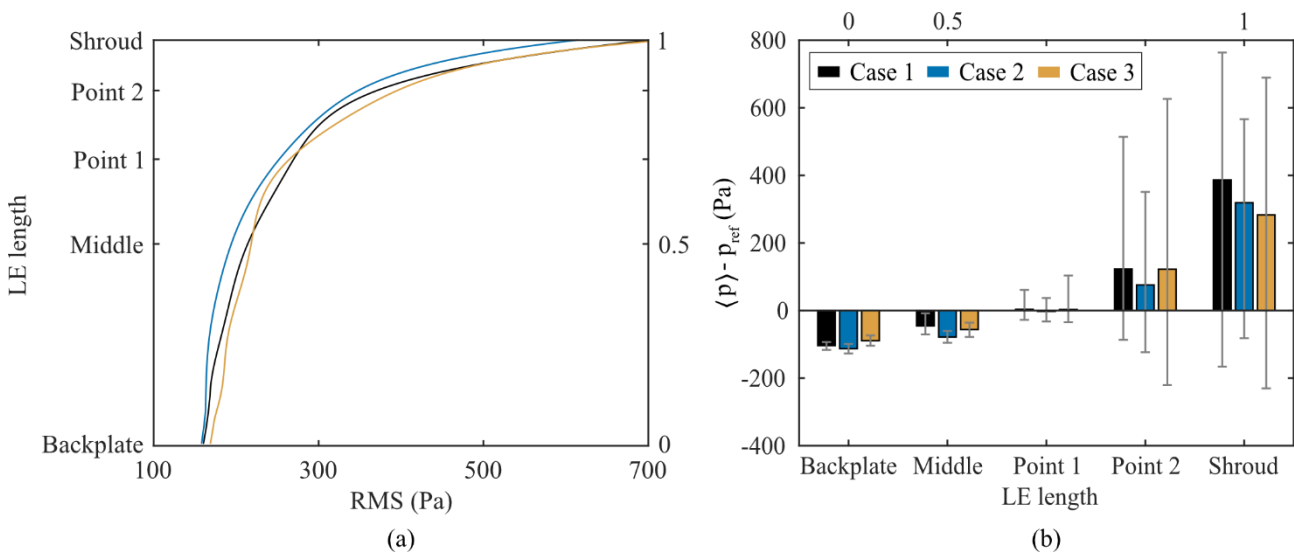(a)   (b)

Figure 6. a) The RMS of the pressure fluctuations for 12 fan revolutions, on one blade at the monitoring line; b) the time-average pressure and error bars showing the minimum and maximum pressure

Figure 7 shows the time history of the surface pressure for all cases at point 2 during 12 fan periods. The dashed lines indicate the average value for each case and as illustrated in Figure 6b, it is lowest for Case 2. For Cases 1 and 3, pressure fluctuations with large amplitudes and high frequencies are observed. Fluctuations are also obvious for Case 2, but the amplitudes are smaller. Moreover, a periodic low-frequency fluctuation in relation to the fan rotation is seen for Case 2, which was also found in [20]. For Cases 1 and 3, there is no clear periodic low-frequency fluctuation. For all the cases, the maximum positive fluctuations are larger than the magnitude of the negative ones. This indicates that the pressure peaks do not happen as frequently for each blade.
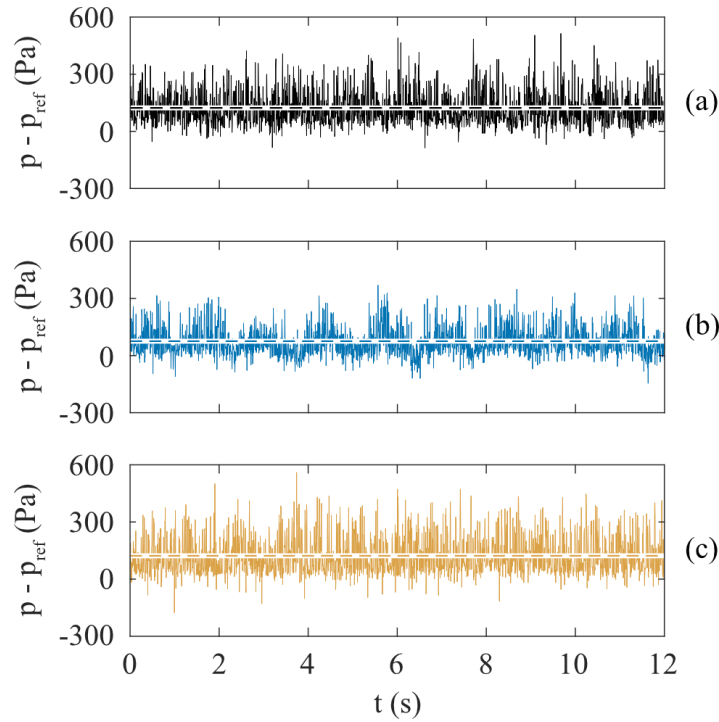

Figure 7. The time history of surface pressures along the BLE at point 2 a) Case 1, b) Case 2, and c) Case 3. The dashed lines indicate the average value for each case

The contours of the velocity magnitudes, $|v_R|$, (eq. 1) in the y-z plane (see Figure 1) and the streamlines of the relative velocity vectors in a plane above the blades (near the fan inlet) are shown for all cases in Figure 8. Note that the axial velocity component along the fan rotation axis is excluded from the vectors. For Cases 1 and 3, there are regions with large velocity magnitudes near the shroud. These regions appear periodically in relation to the blade positions. These regions cannot be observed for Case 2. This suggests that the flow near the shroud is highly fluctuating due to the gap turbulence and that Case 2 has less turbulence above the blades (near the fan inlet).

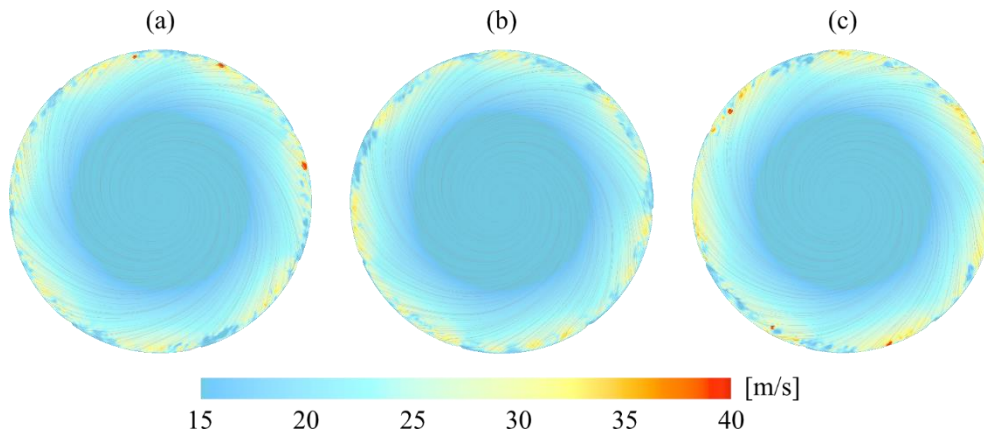$$|v_R| = \sqrt{v_y^2 + v_z^2} \qquad\qquad (1)$$

Figure 8. Instantaneous velocity magnitudes $|v_R|$ visualized in Plane 1: a) Case 1, b) Case 2, and c) Case 3

In the previous studies of Case 1 [16, 20], it was shown that SPL for the tonal frequency, BPF, was best predicted upstream of the fan. The SPL predicted upstream of the fan (microphone M1) for the tonal frequency BPF, is compared between the cases in Figure 9. Cases 1 and 3 have almost the same BPF amplitude. The lowest BPF amplitude has Case 2, where the level has decreased by 5.7 dB compared with Case 1. These results agree with the results from Figures 6-8, where Case 2 had the lowest surface pressure on the BLE.
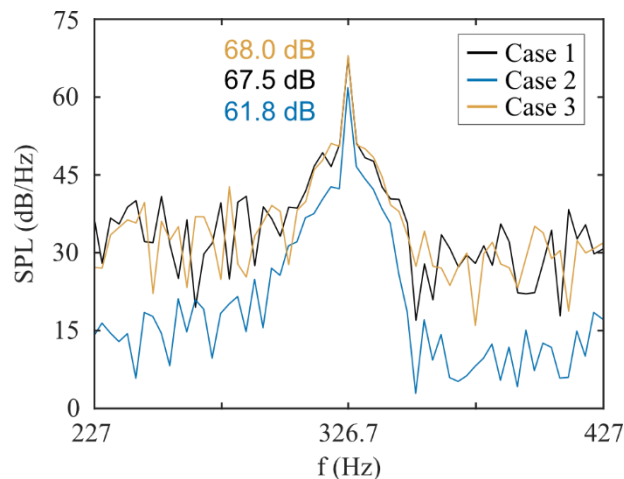

Figure 9. SPL of the sound upstream of the fan. The tonal frequency BPF = 326.7 Hz

The results of the surface pressure fluctuations at the BPF are illustrated for the three cases in Figure 10. Here, only magnitudes above 99 dB/Hz are visualized with colorful contours. The location of the highest surface pressure fluctuations is at the same position (the BLE close to the shroud) for all cases. The differences are the magnitude and the size of the area with high magnitude. Case 1 and Case 3 have the largest sound pressure (see Figure 9), they have also the largest area and magnitude for the tonal frequency. The high energy locations are consistent with the surface pressure fluctuations indicated in Figure 6. The high energy is caused by the interaction between inlet-gap vortices associated with the gap turbulence and the BLE [7]. According to Lee [19], the gap gives rise to a local jet, and that the gap velocity increases with decreased gap size. Larger velocity generates more inlet-gap vortices that interact with the BLE, which is also seen in Figure 10. Additionally, small magnitudes are seen at the blade trailing edge close to the shroud in all cases.
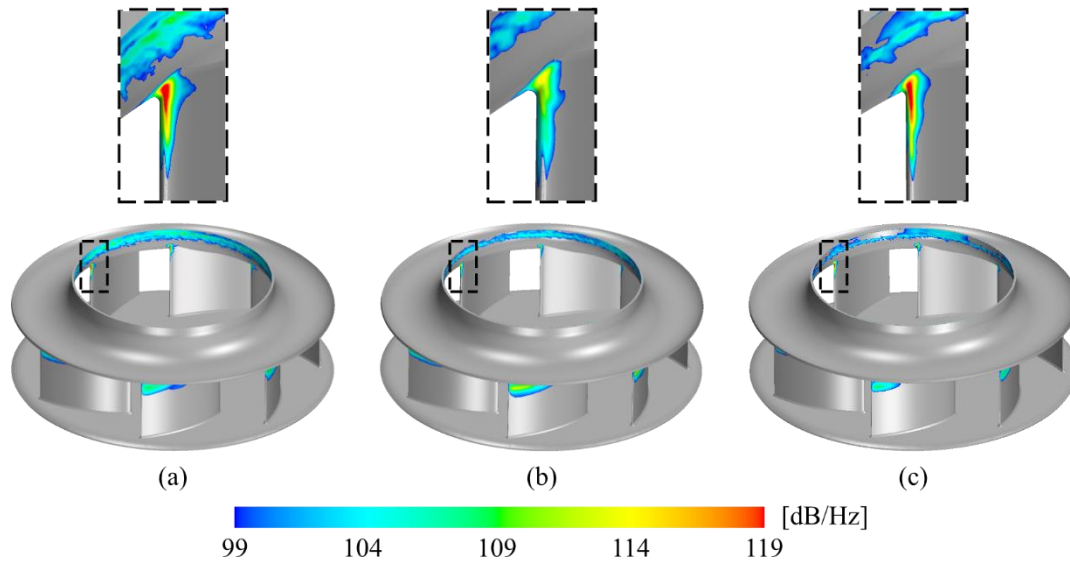
Figure 10. The SPL at BPF (326.7Hz) for surface pressure fluctuations a) Case 1, b) Case 2, and c) Case 3

CONCLUSION

Regions with high vorticity magnitudes are found between the BLE and the gap and ascribed to the turbulence initializing from the inlet gap. The turbulence develops along the shroud and interacts with the BLE. The interaction renders high RMS pressure at the BLE close to the shroud. In addition, the pressure at the shroud fluctuates with high frequency. As the distance to the inlet gap and the shroud increases, the RMS value of the pressure decreases. At the middle position, only small fluctuations are observed.

Spectral analysis is performed for the surface pressure. There are regions with high energy identical to the locations where the gap turbulence evolves and accounts for the impingement on the BLE. Therefore, the gap turbulence dominates the tonal noise generation at the BPF. The spectral analysis is then used to compare the tonal noise at the BPF for three different gap designs.

The three designs show the similar trend of the RMS pressure. The RMS pressure is largest at the shroud and decays when the distance to the gap increases. Moreover, at the position of 20 % blade width to the shroud (point 2 shown in Figure 6), the RMS pressure reaches the smallest value. Case 2 overall has lower RMS amplitudes at all positions, compared to the other cases.

Case 2 has the lowest tonal noise at the BPF. This agrees with the observations on the pressure fluctuations. The spectral analysis also indicates that Case 2 has the lowest magnitude the BLE close to the shroud for all cases. By redesigning the gap, the tonal noise at the BPF is reduced effectively.

ACKNOWLEDGMENTS

REFERENCES

[1] B. Berglund, T. Lindvall, and D. Schwela – *New guidelines for community noise.* Noise Vib. Worldwide, 31:24-29, **2000**.

[2] M. Azimi – *Noise reduction in building using sound absorbing materials.* J. Archit. Eng. Technol. **2017**.

[3] C. Hariharan and M. Govardhan – *Effect of inlet clearance on the aerodynamic performance of a centrifugal blower.* International Journal of Turbo and Jet Engines, 33: 215-228, **2016**.

[4] D. Wolfram and T.H. Carolus – *Experimental and numerical investigation of the unsteady flow field and tone generation in an isolated centrifugal fan impeller.* Journal of Sound and Vibrations, 329:4380-4397, **2010**.

[5] M. Sanjosé and S. Moreau – *Direct noise prediction and control of an installed large low-speed radial fan.* European Journal of Mechanics, 61:235-243, **2017**.

[6] R. Schaefer and M. Boehle – *Influence of the mesh size on the Aerodynamic and Aeroacoustics of a Centrifugal Fan using Lattice-Boltzmann Method.* 23rd International Congress on Acoustics in Aachen, 1882-1889, **2019**.

[7] M. Ottersten, H.-D. Yao, and L. Davidson – *Tonal noise of voluteless centrifugal fan generated by turbulence stemming from upstream inlet gap.* Phys. Fluids, 33, **2021**. https://doi.org/10.1063/5.0055242

[8] M.L. Shur, P.R. Spalart, M.K. Strelets, and A.K. Travin – *A Hybrid RANS-LES Approach with Delayed-DES and Wall-Modelled LES Capabilities.* International J. Heat and Fluid Flow, 29:1638-1649, **2008**.

[9] J.E. Ffowcs Williams and D.L. Hawkings – T*heory relating to the noise of rotating machinery.* Journal of Sound and Vibration, 10:10-21, **1969**.

[10] Siemens PLM Software – *STAR-CCM+ User Guide.* Version 12.04, **2017**.

[11] S. Salunkhe, O.E Fajri, S. Bhushane, D. Thompson, D. O´Dohety, T. O´Dohety, and A. Mason-Jones – *Validation of tidal stream turbine wake predictions and analysis of wake recovery mechanism.* Journal of Marine Science and Engineering, 7, **2019**.

[12] A. Rynell, G. Efraimsson, M. Chevalier, and M. Åbom – *Inclusion of upstream turbulent inflow statistics to numerically acquire proper fan noise characteristics.* SAE Technical Paper 2016-01-1811, **2016**.

[13] A. Rynell, M. Chevalier, M. Åbom, and G. Efraimsson – *A numerical study of noise characteristics originating from a shrouded subsonic automotive fan.* Applied Acoustics 140:110-121, **2018**.

[14] K.S. Brentner and F. Farassat – *Analytical comparison of the acoustic analogy and Kirchhoff formulation for moving surfaces.* AIAAA J 36:1379-86, **1998**.

[15] W. Neise – *Review of fan noise generation mechanisms and control methods.* In: Proceedings of the Fan Noise 1992 International Symposium, Senlis, France. 45-56, **1992**.

[16] M. Ottersten, H.-D. Yao, and L. Davidson – *Unsteady Simulation of tonal noise from isolated centrifugal fan.* Proceedings of FAN 2018 Symposium, Darmstadt, **2018**.

[17] O. Baris, F. Mendonça – *Automotive turbocharger compressor CFD and extension towards incorporating installation effects.* Proceedings of the ASME Turbo Expo 2011: Power for Land, Sea and Air, **2011**.

[18] H.-D. Yao, L. Davidson, and L.E. Eriksson – *Surface integral analogy approaches for predicting noise from 3D high-lift low-noise wings.* Acta Mech. Sin. 30:326-338, **2014**.

[19] Y. Lee – *Impact of fan gap flow on the centrifugal impeller aerodynamics.* Journal of Fluids Engineering, 132:1-9, **2010**.

[20] M. Ottersten, H.-D. Yao, and L. Davidson – *Numerical and experimental study of tonal noise sources at the outlet of an isolated centrifugal fan.* arXiv:2011.13645, **2020**,